Available online at www.sciencedirect.com
SCIENCE DIRECT
Journal of Membrane Science 277 (2006) 7–17
journal of MEMBRANE SCIENCE
www.elsevier.com/locate/memsci

Pressure, flow, and concentration profiles in open and spacer-filled membrane channels

Arun Subramani [a], Suhan Kim [b], Eric M.V. Hoek [b,*]

[a] *Department of Chemical and Environmental Engineering, University of California, Riverside, CA 92521, USA*
[b] *Department of Civil and Environmental Engineering, University of California, Los Angeles, CA 90095, USA*

Received 27 July 2005; received in revised form 20 September 2005; accepted 3 October 2005
Available online 28 November 2005

Abstract

A finite element model was developed to study momentum and mass transport in cross flow membrane filtration systems with open and spacer-filled channels. Simulated conditions represented a range of membrane desalination applications and considered both open and spacer-filled straight through channels, as well as a geometry representing lab-scale cross flow membrane filtration cells. The finite element model agreed with classical analytical models for pressure drop, fluid shear, and concentration polarization in straight-through open channels at low flux and high cross flow. In simulations of representative lab-scale cross flow membrane filters, stagnant regions at the entrance and exit regions, as well as developing flow lead to significant deviations between analytic model and finite element model results. In spacer-filled channels, axial pressure drops were substantially higher than in open channels, varying by a factor of 2 for different spacer configurations (cavity < zigzag < submerged), while shear rates were on average enhanced, but appeared to create stagnant zones where the filaments contacted the membrane. On average, feed channel spacers reduced the extent of concentration polarization because of the enhanced wall shear rates. However, the stagnant regions (in front and behind some spacer filaments) led to enhanced concentration polarization, which suggests certain spacer designs could promote local scale and cake formation in spiral wound elements.

Keywords: Concentration polarization; Reverse osmosis; Finite element; Spacers; Modeling; Film theory

1. Introduction

Concentration polarization is an important factor that limits its separation performance in nearly all cross flow membrane filtration processes [1]. For example, polarization of rejected solutes in reverse osmosis (RO), nanofiltration (NF), and ultrafiltration (UF) separations causes elevated salt concentrations at the membrane–solution interface, which increases solute passage and trans-membrane osmotic pressure [2–5]. In addition, concentration polarization (CP) exacerbates all forms of surface fouling phenomena including scale formation by sparingly soluble mineral salts and cake formation by organics, colloids, and bacteria [6–8]. Therefore, accurate prediction of CP phenomena is critical for design and optimization of these processes.

Concentration polarization is governed by a complex combination of solute properties, membrane properties, and hydrodynamics. From an operational perspective, the cross flow, permeate flux, module geometry, and array configuration determine the extent of concentration polarization. Both permeate flux and cross flow profiles may in turn be altered by the effects of concentration polarization [9,10]. Accurate description of this complex transport problem, involving coupled momentum and mass transfer, requires simultaneous solution of the Navier–Stokes, continuity, and convection–diffusion equations for uncharged solutes [10,11]. Modeling CP phenomena becomes even more complicated for charged and interacting solutes [9,12].

Analytical mass and momentum transport models are reasonably accurate for some cross flow membrane separations, but computational fluid dynamic (CFD) methods are increasingly being used to study pressure, flow, and concentration profiles in RO and NF processes [13]. The main advantage of CFD methods lies in their ability to model complex system geometries and flow patterns through the use of finite element or finite volume numerical approaches. A brief review of recent CFD studies of

* Corresponding author at: Civil and Environmental Engineering Department, 5732G Boelter Hall, PO Box 951593, University of California, Los Angeles, CA 90095-1593, USA. Tel.: +1 310 206 3735; fax: +1 310 206 2222.
E-mail address: hoek@seas.ucla.edu (E.M.V. Hoek).

0376-7388/$ – see front matter © 2005 Elsevier B.V. All rights reserved.
doi:10.1016/j.memsci.2005.10.021

membrane desalination processes is presented to illustrate this point.

Wiley and Fletcher [14] developed CFD models to study the effects of variable solution properties in straight open channels with and without a constant wall velocity. For both cases, CFD predictions of the solute wall concentrations were slightly smaller when compared to analytical and numerical models of Brian [5] and Gill et al. [15]. This CFD study highlighted the importance of changes to viscosity and diffusivity in the concentration boundary layer, and that simplified expressions for the dependence of solution properties on concentration produced grossly inaccurate velocity and concentration profiles.

Cao et al. [16] used a finite volume method to study the flow patterns occurring in channels with net-type turbulence promoters. Enhanced mass transfer was inferred from predicted shear rate, velocity fluctuation, and eddy formation near the membrane surface. Karode and Kumar [17] and Dendukuri et al. [18] also used finite volume methods to study the flow in spacer-filled channels. These authors suggested new feed spacer designs to reduce axial pressure losses, but their study did not consider the effects on concentration polarization.

Geraldes et al. [19] used a finite volume formulation to predict momentum and mass transfer in the feed channels of spiral-wound and plate-and-frame modules. They found excellent agreement between model predictions and experimental data for solute rejection and permeate flux. Later, Geraldes et al. [20,21] used a control volume approach to study the influence of spacer configuration on the flow structure and concentration boundary layer. The study showed the average concentration polarization for filaments adjacent to the membrane is independent of the distance to the channel inlet due to periodic disruption of the concentration polarization layer by the transverse filaments.

Recently, Song and Ma [22] and Ma et al. [23] developed a finite element model to study concentration polarization in spacer-filled channels. Their model was capable of simultaneously solving for solute wall concentration and permeate velocity. The results suggested the formation of stagnant zones where spacer filaments touched the membrane surface, but only filaments attached to the membrane surface were considered in their study.

In this study, simulations were performed to assess pressure, flow, and concentration profiles in open and spacer-filled cross flow channels, which may be representative of lab-scale cross flow RO/NF membrane filters with open and spacer-filled channels. Our first objective was to compare fluid flow, pressure drop, and salt CP phenomena in open channels predicted by a finite element based numerical model and a classic analytical model (film theory). It is of particular interest to determine the relative accuracy of film theory at predicting CP phenomena in lab-scale cross flow membrane filtration units where entrance and exit effects may be significant. Small lab-scale systems are often used to elucidate fundamental mechanisms of RO/NF membrane fouling and scaling; hence, proper interpretation of such mechanistic studies is critically important. The second objective was to utilize the finite element model to determine the impact of spacer configuration on fluid flow, pressure drop, and CP phenomena in spacer-filled channels that are more representative of full scale RO/NF processes.

2. Theory

2.1. Pressure and flow distributions

Cross flow membrane filtration is characterized by a two dimensional flow field comprised of axial (feed) and normal (permeate) velocities. The governing equations needed to obtain the complete velocity profile are the Navier–Stokes and the continuity equations. The Navier–Stokes equations in two dimensions can be written as [24]:

$$v_x\frac{\partial v_x}{\partial x}+\frac{v_y}{H}\frac{\partial v_x}{\partial \lambda}=-\frac{1}{\rho}\frac{\partial p}{\partial x}+\nu\left(\frac{\partial^2 v_x}{\partial x^2}+\frac{1}{H^2}\frac{\partial^2 v_x}{\partial \lambda^2}\right), \tag{1a}$$

$$v_y\frac{\partial v_y}{\partial x}+\frac{v_y}{H}\frac{\partial v_y}{\partial \lambda}=-\frac{1}{\rho}\frac{\partial p}{\partial y}+\nu\left(\frac{\partial^2 v_y}{\partial x^2}+\frac{1}{H^2}\frac{\partial^2 v_y}{\partial \lambda^2}\right). \tag{1b}$$

The continuity equation for incompressible flow is:

$$\frac{\partial v_x}{\partial x}+\frac{1}{H}\frac{\partial v_y}{\partial \lambda}=0. \tag{2}$$

In Eqs. (1) and (2), v_x and v_y are the axial and transverse velocity components, respectively, H the full channel height, ρ the fluid density, μ the fluid viscosity, and λ (=y/H) is the dimensionless channel height. Boundary conditions needed to solve these equations are [25,26]:

$$v_x(x,0)=0, \tag{3a}$$

$$v_x(x,1)=0, \tag{3b}$$

$$v_y(x,0)=v_w, \tag{3c}$$

$$v_y(x,1)=0. \tag{3d}$$

Velocity and pressure profiles in the membrane module can be obtained by solving the equations of motion with the above boundary conditions.

Pressure drop through a slit with two permeable walls can be determined analytically from:

$$\Delta P=\left(\frac{1}{2}\rho\bar{u}^2\right)\left(\frac{24}{Re}-\frac{648}{35}\frac{Re_w}{Re}\right)\left(1-\frac{2Re_w}{Re}\frac{x}{h}\right)\left(\frac{x}{h}\right), \tag{4a}$$

assuming a constant wall velocity [24,27]. This expression can be simplified for the case of impermeable walls ($Re_w=0$) to obtain the pressure drop through a slit with two impermeable walls (i.e., Poiseuille flow) as follows:

$$\Delta P=\left(\frac{1}{2}\rho\bar{u}^2\right)\left(\frac{24}{Re}\right)\left(\frac{x}{h}\right) \tag{4b}$$

In Eq. (4) Re is the cross flow Reynolds number ($Re=\bar{u}(4h)/\nu$; $2h=H$) and Re_w is the Reynolds number at the channel walls ($Re_w=v_w h/\nu$; $v_w=v_y$ at $\lambda=0, 1$).

2.2. Concentration polarization

At steady state, the convective flux of solute towards the membrane minus the convective and diffusive fluxes of solute away from the membrane must equal the solute flux through the membrane. When axial diffusion is neglected, the two-dimensional, steady state convection–diffusion equation is written as:

$$v_x \frac{\partial c}{\partial x} + \frac{v_y}{H}\frac{\partial c}{\partial \lambda} = \frac{D}{H^2}\frac{\partial^2 c}{\partial \lambda^2}, \tag{5}$$

where D is the solute diffusivity and c is the solute concentration. Concentration profiles in the membrane module can be obtained by solving the steady-state convection–diffusion equation with boundary conditions:

$$c = c_0 \quad \text{at } x = 0, \tag{6a}$$

$$\frac{1}{H}\frac{\partial c}{\partial \lambda} = \frac{v_w}{D} R c_w \quad \text{at } \lambda = 1 \text{ and } \lambda = 0. \tag{6b}$$

The rejection coefficient, R, is introduced at the membrane–solution interface to account for incompletely rejected solutes. For the case of a cross flow membrane filter with only one permeable wall, $\partial c/\partial \lambda = 0$ at the impermeable wall.

Analytical models are often used to describe concentration polarization by neglecting axial solute convection near the membrane surface. Such models are based on boundary layer theory and often referred to as 'film theory' models [28,29]. Integrating a one dimensional convection–diffusion mass balance from the membrane surface out to a finite mass boundary (film) layer thickness, δ, yields a relationship between solute concentration, solute diffusivity, film layer thickness, and permeate water flux:

$$\frac{c_w - c_p}{c_b - c_p} = \exp\left(\frac{v_w \delta}{D}\right). \tag{7}$$

The film layer thickness for laminar flow in a slit is determined from a classic solution for channel flow with soluble or rapidly reacting walls [30].

Assuming constant fluid viscosity and solute diffusivity, a local mass transfer coefficient is given by [31,32]:

$$k(x) = \frac{D}{\delta(x)} = 0.538\left(\frac{\dot{\gamma}_w D^2}{x}\right)^{1/3}, \tag{8}$$

where $\dot{\gamma}_w$ ($=\partial u/\partial y$ at $\lambda = 0, 1$) is the wall shear rate. For Poiseuille flow through a slit, the wall shear rate is given by $3\bar{u}/h$, where $\bar{u}$ is $1.5u_{max}$. Eq. (8) derives from a simple balance between axial convection and normal diffusion within a developing concentration boundary layer, but there is no influence of the normal velocity on the film layer thickness.

Combining Eqs. (7) and (8) with the definition of intrinsic solute rejection, R ($=1 - c_p/c_w$), provides a convenient expression for the wall concentration [1,7]:

$$c_w = c_b\left[1 - R + R\exp\left(\frac{v_w}{k}\right)\right]^{-1}. \tag{9}$$

A key limitation of all film theory-based models is the assumption that the transverse component of convection (i.e., permeate velocity) does not influence the boundary layer thickness, δ. However, these simple analytical models can be extended to describe concentration polarization in spacer-filled and tubular channels by using Sherwood number correlations of the form $Sh = aRe^b Sc^c (d_H/L)^d$ [33–35]. These semi-empirical mass transfer correlations are adequate for quick, approximate predictions of mass transfer in real membrane filtration processes.

2.3. Separation performance

In RO and NF processes, the driving force for permeation is the difference between the trans-membrane hydraulic, Δp, and osmotic, $\Delta\pi$, pressures. Thus, the local permeate flux is described by

$$J_w = A(\Delta p - \Delta\pi), \tag{10}$$

where A is the pure water permeability of the membrane and the permeate flux, J_w, describes the normal fluid velocity at the channel wall, v_w. The trans-membrane osmotic pressure is:

$$\Delta\pi = f_{os}(c_w - c_p) = f_{os} R c_w, \tag{11}$$

where R is the intrinsic solute rejection of membrane. In Eq. (11), c_w and c_p are the solute concentrations at the channel wall (membrane surface) and in the permeate, respectively, and f_{os} converts solute concentration to an osmotic pressure [36]. Local solute flux through a membrane is often described by an equation of the form:

$$J_s = B(c_w - c_p) = B R c_w, \tag{12}$$

where B is the solute permeability coefficient. The ratio of solute concentration at the channel wall to that in the bulk is known as the concentration polarization modulus, CP, and is determined from Eq. (9). Eqs. (9)–(12) link concentration polarization to the water and solute fluxes, thus highlighting the paramount role of CP phenomena in RO/NF separations.

2.4. Numerical finite element (FE) simulations

A commercial finite element solver (FEMLAB 3.0, Comsol Inc., Sweden) was used to solve the differential transport equations given above. The underlying mathematical structure by which FEMLAB operates is a system of PDEs, which can be represented in coefficient form, general form, or weak form. In this study, PDEs were represented in the general form, which is intended for non-linear problems. The finite element method is run with adaptive meshing and error control. A stationary non-linear solver was used to solve the time independent equations of motion. A maximum number of 25 iterations were used along with a non-linear tolerance of 10^{-6}. Since finite element simulations are limited by mesh accuracy and because concentration polarization occurs within a thin boundary layer, extremely high resolution meshing was employed near the membrane surface. More than 25,000 elements were used for meshing the entire domain of interest. Simulations were performed on a single processor Pentium® 4, 3 GHz, 2 GB laboratory computer (Precision Workstation 360, Dell Inc., USA).

3. Results and discussion

3.1. Validating the finite element model

Accuracy of finite element (FE) model predictions was tested against classic analytical models of momentum transport in membrane modules, i.e., those of Poiseuille [29] and Berman [24], for channels with zero and two permeable walls. A channel with one permeable wall was also simulated by the FE model. The geometric domain modeled for these tests was a 2-m long slit with a 1-mm channel height. Fig. 1a compares the pressure drop predicted by the FE model and Eq. (4), for a cross flow velocity of 0.1 m s^{-1} ($Re = 200$) and permeation velocity of 8×10^{-6} m s^{-1}. The FE model exactly reproduces the axial pressure drops for a channel with impermeable walls (i.e., Poiseuille flow) and the channel with two permeable walls (Berman's solution). The pressure drop for a channel with a single permeable wall is intermediate and equal to the average of Poiseuille's and Berman's pressure drops.

All simulations were performed using a high resolution of meshing close to the membrane surface, which has been shown to be important [26]. To avoid potential error due to improper meshing, the number of meshing elements in the geometrical domain was increased until a stable solution (<0.1% difference) was obtained. The geometric domain modeled for these tests was a 7.6-cm long slit with a 1-mm channel height. Other conditions used for the simulation were a cross flow velocity of 0.2 m s^{-1}, permeation velocity of 8×10^{-6} m s^{-1}, solute diffusivity of 1.611×10^{-9} m s^{-1}, and intrinsic solute rejection of 90%. The channel average CP modulus was determined by integrating the concentration at the permeable wall (i.e., the membrane) over the entire channel. Fig. 1b shows the predicted CP modulus is stable when more than ~10,000 elements were used. A similar analysis was performed for each simulation. Generally, more than 25,000 elements were employed for all simulations.

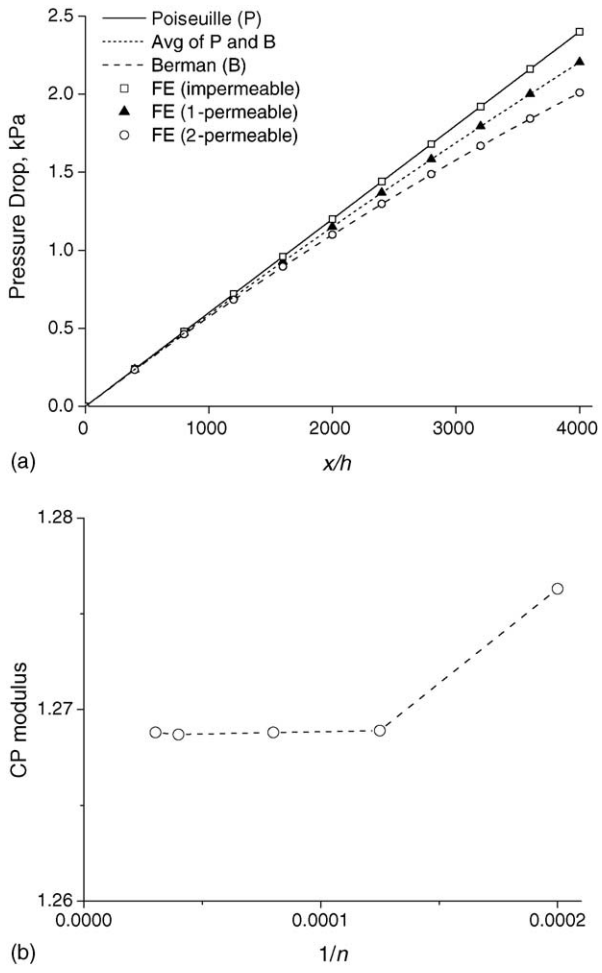

Fig. 1. Axial pressure drop predicted by finite element and analytical models (a) and effect of meshing on predicted CP modulus (b).

3.2. Simulated channel geometries

Fig. 2 depicts the geometrical domains used in subsequent simulations of momentum and mass transport in: (a) a straight through open slit and (b) an actual lab-scale cross flow membrane filter described elsewhere [37,38]. Both simulated channels are 7.62 cm in length with channel height of 1 mm, and each has only one permeable wall. The channel in Fig. 2a represents a theoretical straight through channel, where the flow profile may be assumed fully developed at the channel entrance or not. Alternatively, in Fig. 2b there may be significant stagnant and transitional flow around the entrance and exit regions. This type of geometry and flow is also characteristic of other lab-scale cross flow membrane filters [4].

The three spacer configurations simulated in this study—cavity, submerged, and zigzag—are depicted in Fig. 3a–c, respectively. In all the cases studied, a ladder-type arrange-

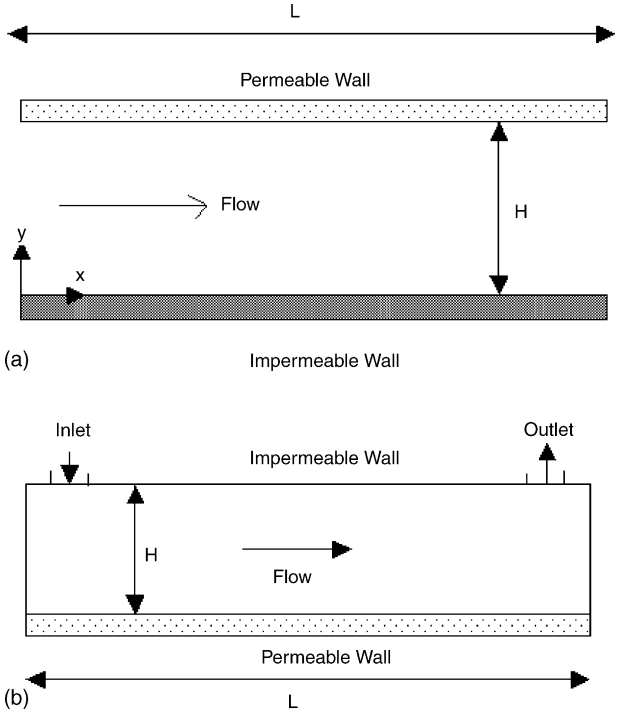

Fig. 2. Illustration of: (a) straight through channel and (b) simulated lab-scale cross flow membrane filtration (CFMF) channel. Flow is from left to right.

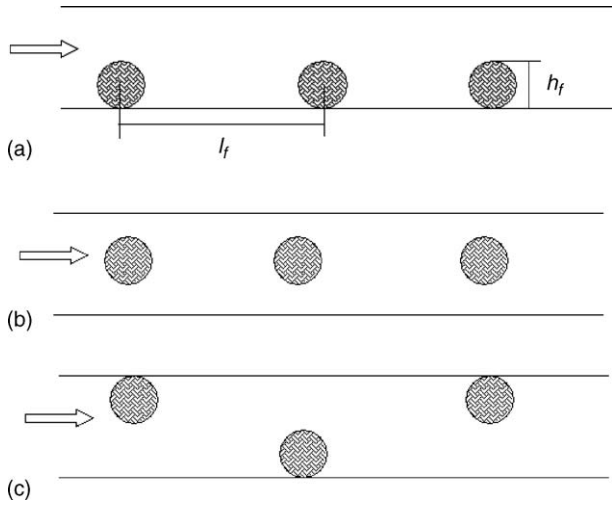

Fig. 3. Illustration of transverse spacer filament locations in straight through CFMF channels with: (a) cavity, (b) submerged, and (c) zigzag spacer configurations. Flow is from left to right.

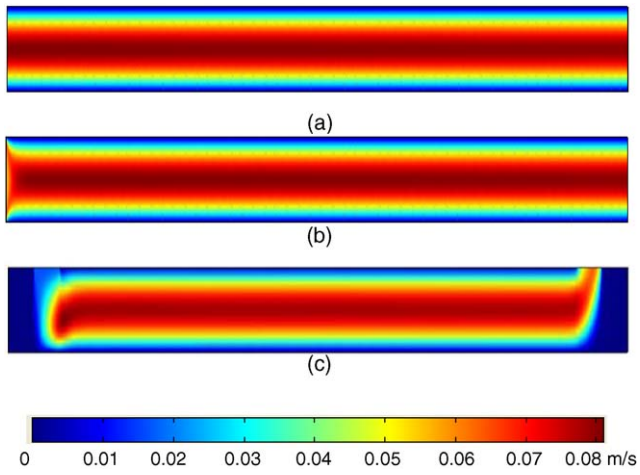

Fig. 4. Illustrations of fluid flow in: (a) a straight through open channel with fully developed flow at inlet, (b) a straight through open channel with undeveloped flow at inlet, and (c) a simulated lab-scale CFMF channel. Flow is from left to right.

ment was assumed so that only the transverse filaments were considered in our two-dimensional simulations. The distance between all transverse filaments (l_f) was set at 4.5 mm and the height (diameter) of cylindrical filaments (h_f) was set at 0.5 mm (half the channel height). In all spacer-filled channel simulations, the permeable wall was located on the top of the cross flow channel. Entrance and exit effects were not investigated. The potential impact of axially oriented filaments (parallel to the flow direction) on pressure drop and fluid flow phenomena was not considered.

3.3. Pressure drop in open and spacer-filled channels

Feed channel spacers generally enhance mixing and reduce (rejected) solute concentration near the permeable wall, but they also increase the axial pressure drop [33–35]. The pressure drops per unit length for a straight through open channel, a lab-scale cross flow membrane filter, and three (straight through) spacer-filled channels at several different inlet velocities are shown in Table 1. Common simulation conditions used were permeation velocity 8×10^{-6} m s^{-1}, channel length of 0.0762 m, channel height of 1 mm, and 13 transverse filaments placed along the channel. In general, the axial pressure drop is attributed to be momentum losses due to abrupt changes in the flow direction, viscous drag, and form drag [18]. In the lab-scale channel, the stagnant zones at the entrance and exit slightly reduced the pressure drop per unit length from that of a straight through channel with the same total length. Spacer-filled channels produced higher pressure drops than both the open and lab-scale channels, but increased according to the order: cavity < zigzag < submerged.

Similar results were found by Cao et al. [16] wherein the pressure drop was slightly higher for a zigzag spacer than for a cavity spacer. Although the filaments are identical in size and shape, the form and viscous drag differ because the placement of sequential filaments in the axial flow field determines the fluid approach velocity. For cavity spacers the fluid takes the least tortuous path, i.e., fewest changes in flow direction, whereas, for zigzag spacers the fluid takes the most tortuous path. However, the filament approach velocity was highest for submerged spacers because they are placed at the channel center where the fluid velocity was highest. For example, when filament size was decreased by 10%, the pressure drop decreased by about 20% for all three spacers configurations assuming identical hydrodynamic conditions. This is a general trend because less momentum loss occurs in more open channels, which leads to lower pressure drop.

3.4. Fluid flow in open channels

Fig. 4 presents representative velocity distributions predicted by the FE model for: (a) a straight through channel (Fig. 2a) with fully developed flow assumed at the inlet, (b) a straight through channel without assuming fully developed flow at the inlet, and (c) the lab-scale cross flow membrane filtration channel (Fig. 2b)

Table 1
Axial pressure drops in open, lab-scale, and spacer-filled channels

u (m s^{-1})	h_f (mm)	Open (kPa m^{-1})	Lab-scale (kPa m^{-1})	Cavity (kPa m^{-1})	Zigzag (kPa m^{-1})	Submerged (kPa m^{-1})
0.025	0.500	0.33	0.28	0.58	0.60	1.04
0.040	0.500	0.54	0.46	1.02	1.06	1.76
0.100	0.500	1.40	1.27	3.32	3.43	5.51
0.200	0.500	2.94	2.93	8.59	8.62	14.51
0.200	0.450	2.94	2.93	6.79	6.88	11.74

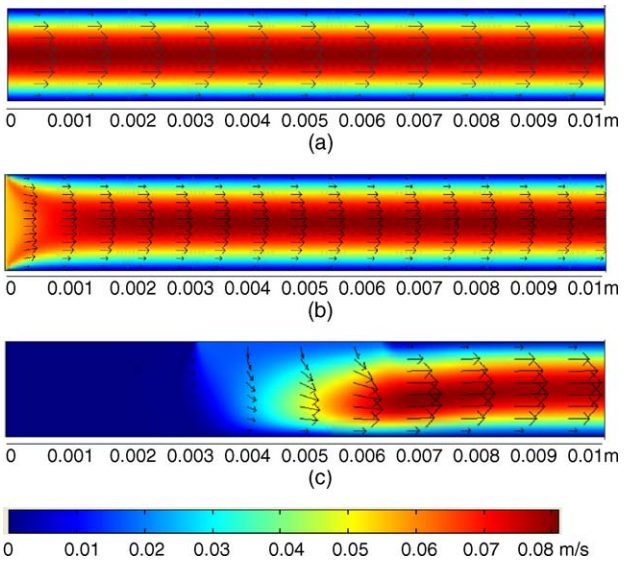

Fig. 5. Velocity vector diagrams and fluid flow at the channel entrance for: (a) a straight through open channel with fully developed flow at inlet, (b) a straight through open channel with undeveloped flow at inlet, and (c) a simulated lab-scale CFMF channel. Flow is from left to right.

with no flow profile assumed. Common simulation conditions are cross flow velocity of 0.05 m s^{-1} ($Re = 100$), one permeable wall, and permeation velocity of 8×10^{-6} m s^{-1}. The finite element simulations are clearly capable of identifying entrance and exit effects, which result in stagnant zones near the entrance and exit as well as a significant development length.

Fig. 5 presents representative velocity distributions and velocity vectors near the entrance region for identical conditions as plotted in Fig. 4. The stagnant flow in the entrance region of the channel (dark blue regions) may lead to locally elevated polarization and fouling phenomena, and the increased development length may significantly alter downstream hydrodynamic conditions, concentration polarization, and solute rejection. Therefore, it is important to consider entrance and exit effects when interpreting concentration polarization phenomena in small lab-scale systems. In addition, fouling and scaling data obtained from such systems will likely be influenced by the same hydrodynamic phenomena.

To determine the effect of developing flow on wall shear rates, simulations were performed in a straight through channel with (FE1) and without (FE2) fully developed flow at the channel entrance. Axial velocities were extracted at 0.01 mm above the permeable wall and at several locations along the channel. The velocity profile is assumed approximately linear within this thin layer equal in thickness to 1% of the channel height. Wall shear rates predicted for cross flow velocity of 0.1 m s^{-1} and permeation velocity 8×10^{-6} m s^{-1} are given in Table 2. Finite element determined wall shear rates are compared to the analytical prediction of shear rate, $\dot{\gamma}_w = 3\bar{u}/h$, which is valid for Poiseuille flow. When assuming fully developed flow at the entrance, finite element predictions fall within 2% of the analytical expression. However, shear rates are much higher in the entrance region and slightly lower at the exit.

Table 2
Effect of entrance condition on wall shear rates in straight through open channels

x/L	Analytical	FE1	Deviation (%)	FE2	Deviation (%)
0.003	600	594	−1.0	1331	54.9
0.009	600	594	−1.0	838	28.4
0.013	600	594	−1.0	748	19.8
0.100	600	594	−1.0	570	−5.2
0.200	600	594	−1.1	569	−5.5
0.400	600	593	−1.2	568	−5.6
0.600	600	592	−1.3	567	−5.7
0.800	600	592	−1.4	567	−5.9
1.000	600	591	−1.6	566	−6.0

FE1: fully developed flow at inlet (average wall shear rate = 593 s^{-1}) and FE2: developing flow at inlet (average wall shear rate = 661 s^{-1}).

Finite element simulated wall shear rates at different permeate fluxes are compared to Poiseuille flow shear rates in Table 3. A constant cross flow velocity of 0.3 m s^{-1} ($Re = 600$) was employed. Except at the channel entrance, finite element wall shear rates fell within 3% of the Poiseuille flow values. This suggests that at realistic permeate fluxes the Poiseuille flow expression for shear rate is reasonable, when entrance effects are negligible, such as in a long filtration channel. The Poiseuille flow expression is much less accurate when fully developed flow is not assumed at the inlet. In the developing region, the flow is not parabolic and the wall shear rate is higher than predicted by the analytical expression. Moreover, the shear rate predictions are in greater error near the end of the channel due to the declining cross flow.

The effect of cross flow velocity on wall shear rates was studied and representative profiles are plotted in Fig. 6a for a straight through open channel at cross flow velocities of 0.1 m s^{-1}

Table 3
Effect of flux on wall shear rates in straight through open channels

x/L	Analytical	FE, 8 gfd	Deviation (%)	FE, 16 gfd	Deviation (%)	FE, 32 gfd	Deviation (%)
0.003	1800	6988	288.2	6988	288.2	6989	288.3
0.009	1800	3620	101.1	3621	101.2	3622	101.2
0.013	1800	3159	75.5	3159	75.5	3160	75.6
0.100	1800	1900	5.6	1900	5.6	1901	5.6
0.200	1800	1783	−0.9	1784	−0.9	1784	−0.9
0.400	1800	1764	−2.0	1764	−2.0	1763	−2.0
0.600	1800	1763	−2.1	1762	−2.1	1762	−2.1
0.800	1800	1763	−2.1	1762	−2.1	1760	−2.2
1.000	1800	1757	−2.4	1756	−2.5	1753	−2.6

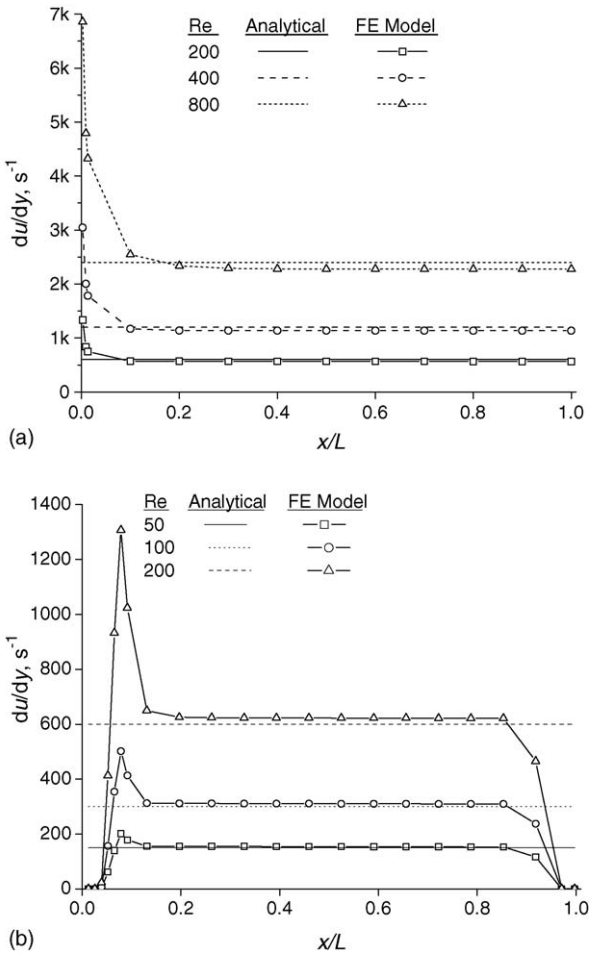

Fig. 6. (a) Wall shear rates predicted by finite element model in a straight through open channel and (b) wall shear rates predicted by assuming Poiseuille flow profile and by finite element model in simulated lab-scale CFMF channel.

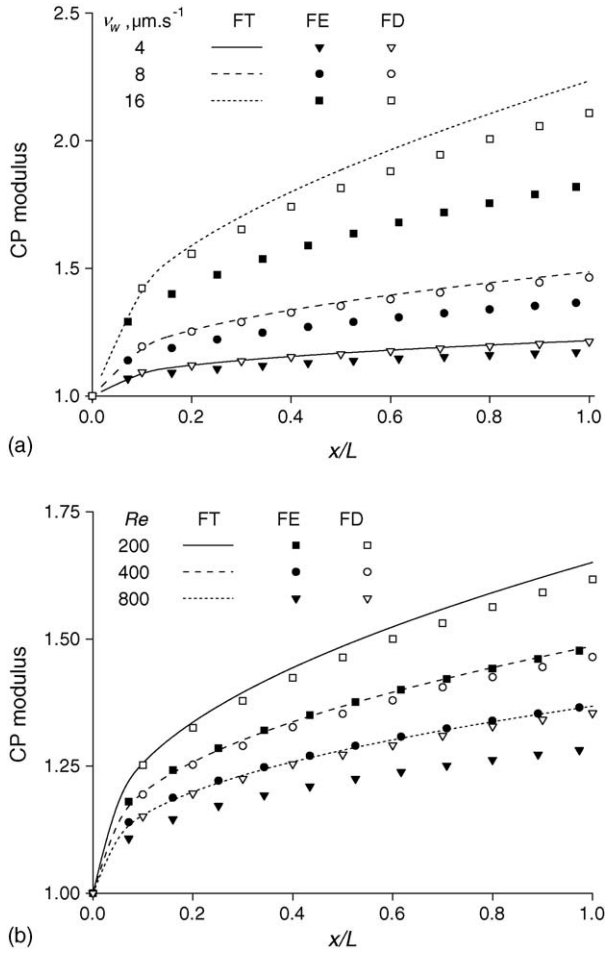

Fig. 7. Concentration polarization (CP) modulus predicted by finite element (FE), film theory (FT), and finite difference (FD) models in straight through open CFMF channels. In (a) different permeation velocities are plotted and in (b) different cross flow velocities are plotted.

($Re = 200$), 0.2 m s^{-1} ($Re = 400$), and 0.4 m s^{-1} ($Re = 800$) and permeation velocity 8×10^{-6} m s^{-1}. As expected, the finite element predicted wall shear rates for straight through channels are significantly higher at the channel entrance. Since the entrance effect is directly proportional to feed flow rate, lower feed flow velocities yield smaller entrance effects, and thus, wall shear rates predicted by the analytical solution are more accurate at low Reynolds number flows.

Wall shear rates were determined for the simulated lab-scale filter and plotted in Fig. 6b for cross flow velocities of 0.025, 0.05, and 0.1 m s^{-1} and permeation velocity 8×10^{-6} m s^{-1}. Due to the stagnant zones at both ends of the lab unit, the wall shear rates are insignificant at the extreme channel ends, which could result in excessively high concentration polarization, scale formation, and cake formation. However, the rapid change in flow direction at the inlet of the thin channel causes a severe spike in the shear rate. The predicted wall shear rates level off—through the middle 60–80% of the channel, depending on the cross flow rate—to very near the Poiseuille flow values until exit effects cause the shear to rapidly stagnate.

3.5. Concentration polarization in open channels

Dimensionless solute wall concentrations (a.k.a., the "CP modulus") along a straight through open channel (as in Fig. 2a) predicted by the finite element (FE) model assuming fully developed flow at inlet are compared to those of film theory (FT) and a previously published finite difference (FD) numerical model (see reference [31] for details). In Fig. 7a the cross flow velocity is constant at 0.2 m s^{-1} ($Re = 400$), but permeate velocity varies from 4 to 16 μm s^{-1}. At a permeation velocity of 4.0 μm s^{-1}, both film theory and the finite difference model predict the CP modulus to be nearly identical with that predicted by the finite element model. At the higher permeation rates, both the FT and FD models overestimate the CP modulus, particularly toward the end of the channel. The key limitation of both the FT and FD models is the assumption of fully developed flow at the channel entrance. The development length at the cross flow employed is significant, and thus, the fluid flow and solute polarization are not accurately described by this assumption.

Model predictions are also compared for different cross flow conditions ($Re = 200$, 400, and 800) at a constant permeation velocity of 8×10^{-6} m s^{-1} in Fig. 7b. At higher cross flow veloc-

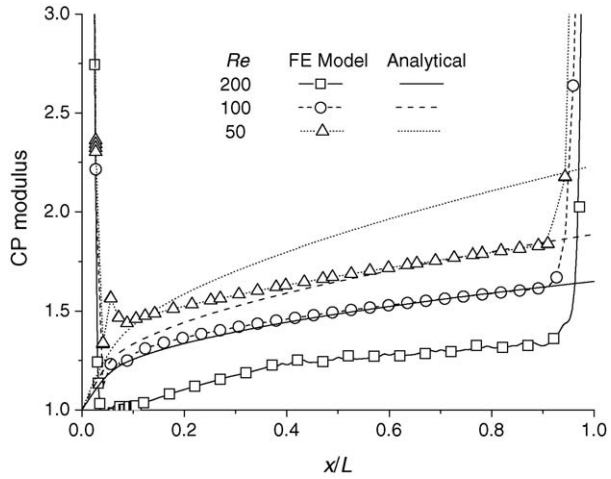

Fig. 8. CP modulus predicted by FE and FT models in simulated lab-scale CFMF channel for constant permeation velocity (8.0 $\mu m\,s^{-1}$) and different cross flow velocities.

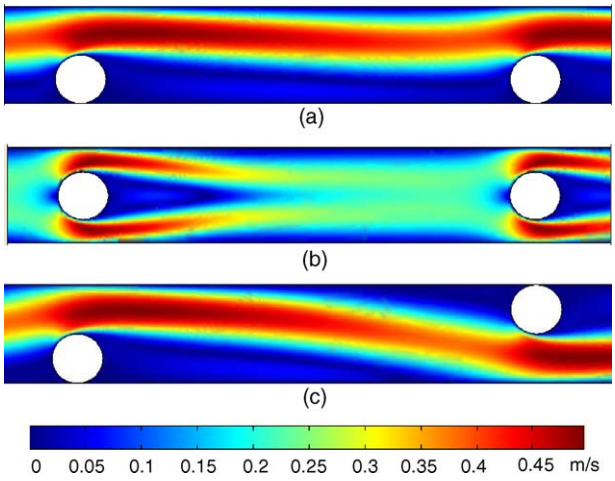

Fig. 9. Illustrations of fluid flow through short sections of spacer-filled channels assuming: (a) cavity, (b) submerged, and (c) zigzag spacer configurations. Scale bar is from 0 (blue) to 0.5 $m\,s^{-1}$ (red). Flow is from left to right.

ities, FT and FD model predictions are closer to finite element predictions, but may over predict concentration polarization by as much as 20%. At lower cross flow velocities, the FT and FD models may over predict the CP modulus by as much as 100%. The finite element simulations perform a rigorous evaluation of the transport equations presented in Eqs. (1), (2), and (5), whereas, film theory neglects the influence of wall permeation on CP layer thickness. In all simulations, a constant wall velocity was assumed, which may be reasonable for short membrane channels with recovery less than 1%—as is the case in most small lab-scale RO/NF modules, but which may not be reasonable for longer membrane channels—as in the case of most full scale RO/NF modules [22].

Although film theory works well in short membrane filtration channels for conditions of low cross flow and low flux, it is severely limited at both higher cross flows and higher permeate fluxes. The primary source of error at high fluxes is the independence of the boundary layer thickness from permeation. At high cross flows (in short channels), entrance and exit effects are likely to cause additional error in predicting concentration polarization. However, in full scale RO and NF modules entrance and exit effects may be relatively negligible. Therefore, it appears reasonable to apply film theory to describe concentration polarization phenomena in straight through, open channels when entrance and exit effects are negligible.

In the lab-scale filter, application of film theory to describe concentration polarization is similarly, but more severely limited. Concentration polarization modulus predictions from film theory and the finite element model are plotted in Fig. 8 for the channel geometry given in Fig. 2b. Simulation conditions used were cross flow velocities of 0.025, 0.05, and 0.1 $m\,s^{-1}$ ($Re = 50$, 100, and 200), and permeation velocity of 8×10^{-6} $m\,s^{-1}$. Due to the abrupt changes in flow direction at the inlet and outlet, flow is not straight through the channel and stagnant zones form at both ends of the channel. Thus, the wall shear rates on the membrane surface are considerably lower near the inlet and outlet, which leads to higher concentration polarization in those regions. However, for the same hydrodynamic conditions, the wall shear rate along a straight through channel is lower, which leads to higher concentration polarization at the membrane surface. If a large permeation velocity is employed, as is often the case in "accelerated fouling experiments", film theory is not likely to provide an accurate description of concentration polarization.

3.6. Fluid flow in spacer-filled channels

Representative flow profiles in spacer-filled channels are shown in Fig. 9 for: (a) cavity, (b) submerged, and (c) zigzag spacer configurations. Common simulation conditions were cross flow velocity 0.2 $m\,s^{-1}$ ($Re = 400$), one permeable channel wall (at the top), and permeation velocity 8×10^{-6} $m\,s^{-1}$. In Fig. 9a, flow stagnates between filaments and most flow occurs above the filaments (closer to the permeable wall). The bulk velocity is increased above the filaments since the fluid is effectively forced to flow through a reduced channel cross-section. For example, in an open channel with cross flow velocity of 0.2 $m\,s^{-1}$ the maximum velocity is 0.3 $m\,s^{-1}$, whereas, the maximum velocity in the cavity spacer-filled channel is 0.5 $m\,s^{-1}$. In addition, this velocity occurs closer to the permeable wall; hence, the wall shear rate will be higher and concentration polarization will be lower.

A representative flow profile for the submerged spacer is shown in Fig. 9b. High velocities are generated at both walls, especially near the cylindrical filaments. However, fluid flow slows around the (forward and rear) stagnation points. A representative flow profile for the zigzag spacer is shown in Fig. 9c. The fluid undergoes a directional shift as it approaches each filament and the flow is stagnant in front and behind each filament. This is particularly problematic for filaments placed on the membrane surface where it is desirable for concentration polarization to be lowest.

Velocity vector diagrams are plotted in Fig. 10 to further illustrate fluid flow in the spacer-filled channels. All three spacer

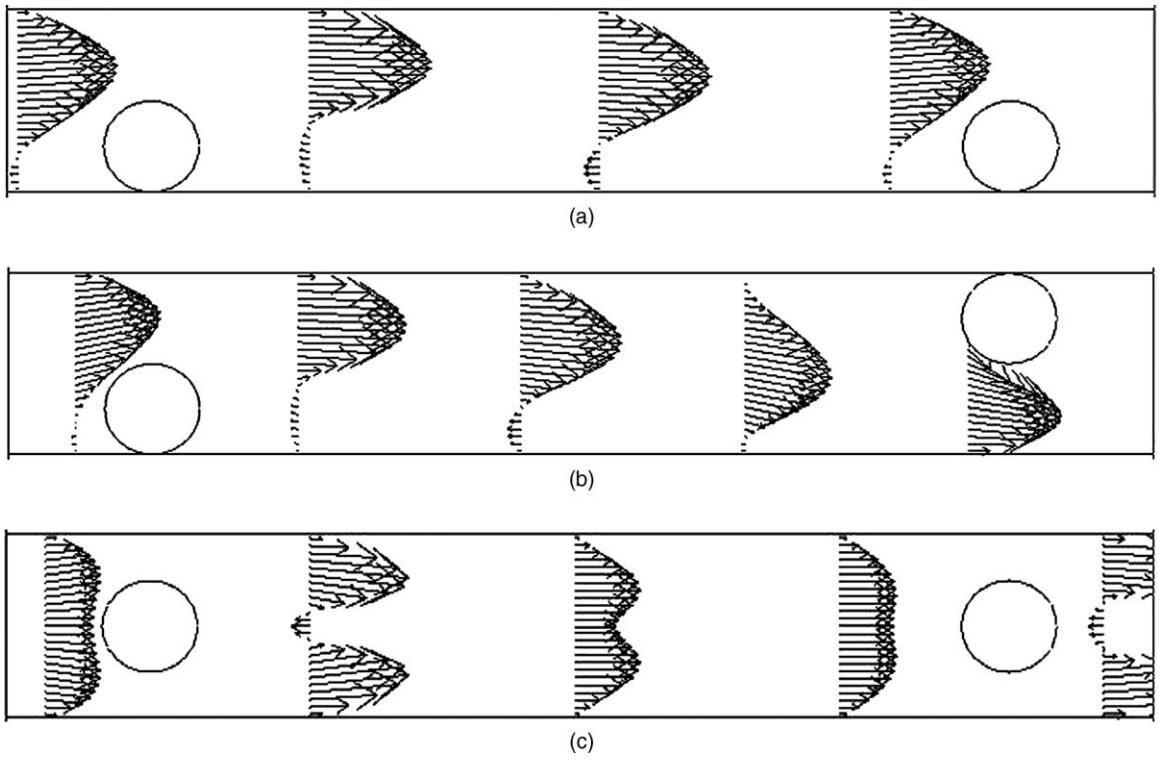

Fig. 10. Velocity vector diagrams for fluid flow through short sections of spacer-filled channels assuming: (a) cavity, (b) zigzag, and (c) submerged spacer configurations. Flow is from left to right.

designs result in a flow reversal behind each filament, but the extent and magnitude of the flow reversal is different for the different spacer designs. Flow reversals lead to locally negative shear stresses due to the formation of eddies [16]. Thus, different spacer configurations lead to different fluid flow patterns, which may locally increase or reduce mass transfer and axial pressure losses (recall Table 1). Although the axial wall velocity appears positive and non-zero at the upper (permeable) wall in Fig. 10 for all three spacer configurations, this is a graphical aberration and the wall velocity is actually zero by definition of the boundary conditions given in Eq. (3).

Local wall shear rates occurring between two consecutive filaments in the channel center are plotted in Fig. 11 for the same simulation conditions used above. Axial velocities were extracted at 0.01 mm above the permeable wall for several locations between the filaments. Wall shear rates were estimated assuming the velocity profile to be linear within this thin layer and are plotted between the two filaments. Cavity and submerged spacers produce higher wall shear rates than the zigzag spacer. The highest shear is produced by the submerged spacers at the filament, but the shear rate drops substantially below that of the cavity spacer and slightly below that of an open channel between the filaments. In the case of cavity and submerged configuration a higher flow region occurs close to the membrane surface enhancing the wall shear rate. The shift in flow direction from filament to filament for the zigzag spacer appears to create more stagnant flow over the permeable wall, than do the submerged and cavity spacers or the open channel. Thus, the solute mass transfer will not be uniform across the membrane surface and will strongly depend on the spacer configuration.

3.7. Concentration polarization in spacer-filled channels

Dimensionless wall concentrations (a.k.a., the "CP modulus") for open and spacer-filled channels are plotted in Fig. 12 for five consecutive filaments located through the middle of the filtration channel. The submerged spacer CP modulus is lowest close to the filament and highest between filaments, but appears to stay at or below the open channel CP modulus throughout. The cavity spacer produces consistently lower solute wall concentrations with smaller amplitude of variation between filaments.

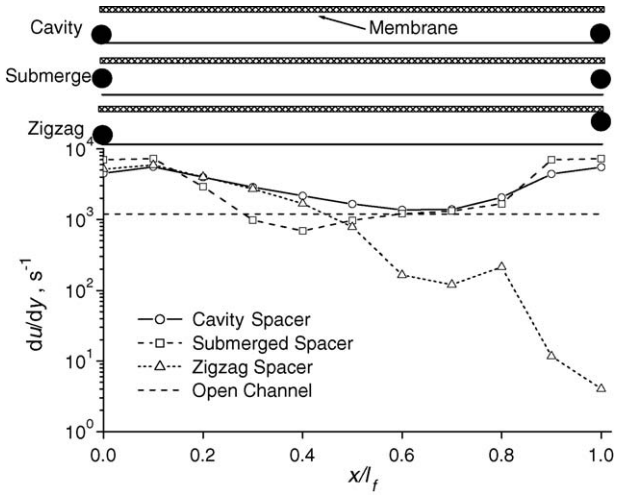

Fig. 11. Wall shear rates between consecutive transverse filaments for channels with cavity, submerged, and zigzag spacer configurations compared to open channel.

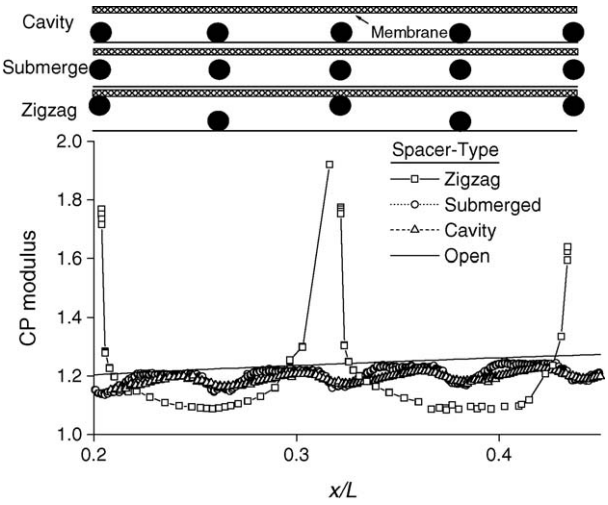

Fig. 12. Comparison of CP modulus between consecutive transverse filaments for channels with cavity, submerged, and zigzag spacer configurations compared to open channel.

Recall from Fig. 11, the cavity spacer did not produce the highest wall shear rates, but they were always above the open channel value. Both the submerged and zigzag spacers produced higher shear at the filaments, as well as lower shear between filaments (than either open channels or cavity spacers). Further, the stagnant zones produced by zigzag spacers lead to a local CP modulus far in excess of an open channel. These local spikes in concentration polarization could act as initiation sites for fouling and scaling. In fact, this result suggests that zigzag spacers could actually lead to more severe fouling and scaling than an open channel.

4. Conclusions

A finite element numerical model was used to study pressure losses, fluid flow patterns, and concentration polarization in open and spacer-filled channels. In straight through open channels, wall shear rates were reasonably described by a simple Poiseuille flow profile; however, at high cross flow velocities entrance effects were non-negligible and downstream shear rates were significantly overestimated. In a more complex flow geometry, which might represent a small lab-scale cross flow membrane filtration device, the wall shear stagnated around the inlet and outlet. Finite element model predictions of rejected solute concentrations compared well with film theory for conditions of low cross flow and low permeate flux in straight through open channels. Analysis of the lab-scale filter geometry confirmed the stagnant regions at the inlet and outlet lead to enhanced concentration polarization. In small lab-scale flow cells, both high cross flows and high permeate fluxes may lead to concentration polarization conditions that can not be predicted by film theory.

Pressure, flow, and CP phenomena were simulated in two dimensions for channels containing different feed spacer configurations. Short channel sections with only one permeable wall were simulated, so the simulated permeate water recovery was negligible. These conditions are most relevant to small lab-scale RO/NF modules; hence, the simulation results may not be applicable to all membrane systems. For all spacer configurations considered (cavity, zigzag, and submerged) the pressure drop was higher and concentration polarization was lower than in an open channel, but the effect varied depending on the nature of flow alteration near the membrane. The two dimensionally simulated zigzag spacer configuration exhibited dramatic fluctuations in concentration polarization due to stagnant zones caused by the directional changes of the flowing fluid, which suggests that zigzag spacers could locally promote fouling and scaling in the stagnant zones. Therefore, the cavity and submerged configurations appear better suited to promote mass transfer under the conditions simulated.

Acknowledgements

Financial support for this work was provided by the United States Environmental Protection Agency (US EPA) through the Desalination Research Innovation Partnership (DRIP), which is managed by the Metropolitan Water District of Southern California. We also thank Professor Yoram Cohen and his research group at UCLA for many valuable discussions about modeling transport phenomena in membrane processes.

Nomenclature

A	solvent permeability coefficient (m Pa^{-1} s^{-1})
B	solute permeability coefficient (mol m^{-2} s^{-1})
c	concentration (mol m^{-3})
d_H	hydraulic diameter
D	diffusivity (m^2 s^{-1})
f_{os}	osmotic coefficient (Pa/mol)
h	channel half-height (m)
H	channel height (m)
J	flux (m s^{-1})
k	mass transfer coefficient (m s^{-1})
L	channel length (m)
P	pressure (Pa)
Q	flow rate (m^3 s^{-1})
R	solute rejection coefficient
Re	cross flow Reynolds number
Re_w	wall (permeate) Reynolds number
Sc	Schmidt number
Sh	Sherwood number
u	axial velocity (m s^{-1})
$\bar{u}$	bulk axial (cross flow) velocity (m s^{-1})
v	normal velocity (m s^{-1})
v_w	permeate velocity at the wall (m s^{-1})
x	axial coordinate
y	normal coordinate
z	transverse coordinate

Greek letters

$\dot{\gamma}_w$	wall shear rate (s^{-1})

δ	film layer thickness (m)
λ	dimensionless channel height, y/H
μ	dynamic viscosity ($kg\,m^{-1}\,s^{-1}$)
ν	kinematic viscosity ($m^2\,s^{-1}$)
π	osmotic pressure (Pa)
ρ	density ($kg\,m^{-3}$)

Subscripts

0	inlet/initial
b	bulk
m	membrane
s	solute
p	permeate
w	wall

References

[1] M. Mulder, Basic Principles of Membrane Technology, Kluwer Academic Publishers, Dordrecht, Netherlands, 1991.

[2] W.F. Blatt, A. Dravid, A.S. Michaels, L. Nelson, Solute polarization and cake formation in membrane ultrafiltration: causes, consequences, and control techniques, in: J.E. Flinn (Ed.), Membrane Science and Technology: Industrial, Biological, and Waste Treatment Processes, Plenum Press, Columbus, Ohio, 1970, p. 47.

[3] M.C. Porter, Concentration polarization with membrane ultrafiltration, Ind. Eng. Chem. Prod. Res. Develop. 11 (1972) 234.

[4] E.M.V. Hoek, A.S. Kim, M. Elimelech, Influence of crossflow membrane filter geometry and shear rate on colloidal fouling in reverse osmosis and nanofiltration separations, Environ. Eng. Sci. 19 (2002) 357.

[5] P.L.T. Brian, Concentration polarization in reverse osmosis desalination with variable flux and incomplete salt rejection, Ind. Eng. Chem. Fund. 4 (1965) 439.

[6] S. Bhattacharjee, G.M. Johnston, A model of membrane fouling by salt precipitation from multicomponent ionic mixtures in crossflow nanofiltration, Environ. Eng. Sci. 19 (2002) 399.

[7] E.M.V. Hoek, M. Elimelech, Cake-enhanced concentration polarization: a new fouling mechanism for salt-rejecting membranes, Environ. Sci. Technol. 37 (2003) 5581.

[8] L.F. Song, M. Elimelech, Theory of concentration polarization in crossflow filtration, J. Chem. Soc., Faraday Trans. 91 (1995) 3389.

[9] S. Bhattacharjee, A.S. Kim, M. Elimelech, Concentration polarization of interacting solute particles in cross-flow membrane filtration, J. Colloid Interf. Sci. 212 (1999) 81.

[10] D. Bhattacharyya, S.L. Back, R.I. Kermode, M.C. Roco, Prediction of concentration polarization and flux behavior in reverse-osmosis by numerical-analysis, J. Membr. Sci. 48 (1990) 231.

[11] K. Madireddi, R.B. Babcock, B. Levine, J.H. Kim, M.K. Stenstrom, An unsteady-state model to predict concentration polarization in commercial spiral wound membranes, J. Membr. Sci. 157 (1999) 13.

[12] S. Bhattacharjee, J.C. Chen, M. Elimelech, Coupled model of concentration polarization and pore transport in crossflow nanofiltration, AIChE J. 47 (2001) 2733.

[13] D.E. Wiley, D.F. Fletcher, Computational fluid dynamics modelling of flow and permeation for pressure-driven membrane processes, Desalination 145 (2002) 183.

[14] D.E. Wiley, D.F. Fletcher, Techniques for computational fluid dynamics modelling of flow in membrane channels, J. Membr. Sci. 211 (2003) 127.

[15] W.N. Gill, D.E. Wiley, C.J.D. Fell, A.G. Fane, Effect of viscosity on concentration polarization in ultrafiltration, AIChE J. 34 (1988) 1563.

[16] Z. Cao, D.E. Wiley, A.G. Fane, Cfd simulations of net-type turbulence promoters in a narrow channel, J. Membr. Sci. 185 (2001) 157.

[17] S.K. Karode, A. Kumar, Flow visualization through spacer filled channels by computational fluid dynamics. I. Pressure drop and shear rate calculations for flat sheet geometry, J. Membr. Sci. 193 (2001) 69.

[18] D. Dendukuri, S.K. Karode, A. Kumar, Flow visualization through spacer filled channels by computational fluid dynamics. II. Improved feed spacer designs, J. Membr. Sci. 249 (2005) 41.

[19] V. Geraldes, V. Semiao, M.N. De Pinho, Flow and mass transfer modelling of nanofiltration, J. Membr. Sci. 191 (2001) 109.

[20] V. Geraldes, V. Semiao, M.N. De Pinho, The effect of the ladder-type spacers configuration in nf spiral-wound modules on the concentration boundary layers disruption, Desalination 146 (2002) 187.

[21] V. Geraldes, V. Semiao, M.N. De Pinho, Concentration polarisation and flow structure within nanofiltration spiral-wound modules with ladder-type spacers, Comput. Struct. 82 (2004) 1561.

[22] L. Song, S. Ma, Numerical studies of the impact of spacer geometry on concentration polarization in spiral wound membrane modules, Ind. Eng. Chem. Res. (2005).

[23] S.W. Ma, L.F. Song, S.L. Ong, W.J. Ng, A 2D streamline upwind petrov/galerkin finite element model for concentration polarization in spiral wound reverse osmosis modules, J. Membr. Sci. 244 (2004) 129.

[24] A. Berman, Laminar flow in channels with porous walls, J. Appl. Phys. 24 (1953) 1232.

[25] C. Kleinstreuer, M.S. Paller, Laminar dilute suspension flows in plate-and-frame ultrafiltration units, AIChE J. 29 (1983) 529.

[26] L.H. Huang, M.T. Morrissey, Finite element analysis as a tool for crossflow membrane filter simulation, J. Membr. Sci. 155 (1999) 19.

[27] S.K. Karode, Laminar flow in channels with porous walls, revisited, J. Membr. Sci. 191 (2001) 237.

[28] H. Schlichting, Boundary-layer Theory, 7th ed., McGraw-Hill Inc., New York, NY, 1979.

[29] R.B. Bird, W.E. Stewart, E.N. Lightfoot, Transport Phenomena, 2nd ed., John Wiley & Sons Inc., 2002.

[30] R.F. Probstein, Physicochemical Hydrodynamics, 2nd ed., John Wiley & Sons, Hoboken, New Jersey, 2003.

[31] S. Kim, E.M.V. Hoek, Modeling concentration polarization in reverse 684 osmosis processes, Desalination 186 (2006) 111–128.

[32] A.L. Zydney, C.K. Colton, A concentration polarization model for the filtrate flux in cross-flow microfiltration of particulate suspensions, Chem. Eng. Commun. 47 (1986) 1.

[33] G. Schock, A. Miquel, Mass-transfer and pressure loss in spiral wound modules, Desalination 64 (1987) 339.

[34] J. Schwinge, D.E. Wiley, A.G. Fane, Novel spacer design improves observed flux, J. Membr. Sci. 229 (2004) 53.

[35] A.R. Da Costa, A.G. Fane, D.E. Wiley, Spacer characterization and pressure drop modelling in spacer-filled channels for ultrafiltration, J. Membr. Sci. 87 (1994) 79.

[36] L. Song, S. Hong, J.Y. Hu, S.L. Ong, W.J. Ng, Simulations of full-scale reverse osmosis membrane process, J. Environ. Eng. ASCE 128 (2002) 960.

[37] S.Y.C. Wang, G. Guillen, E.M.V. Hoek, Direct microscopic observation of microbial adhesion to membranes, Environ. Sci. Technol. 39 (2005) 6461.

[38] S.T. Kang, A. Subramani, E.M.V. Hoek, M.A. Deshusses, M.R. Matsumoto, Direct observation of biofouling in cross-flow microfiltration: mechanisms of deposition and release, J. Membr. Sci. 244 (2004) 151.